Journal of Glaciology

Article

Cite this article: Schroeder DM, Broome AL, Conger A, Lynch A, Mackie EJ, Tarzona A (2021). Radiometric analysis of digitized Z-scope records in archival radar sounding film. *Journal of Glaciology* 1–8. https://doi.org/10.1017/jog.2021.130

Received: 16 April 2021
Revised: 23 November 2021
Accepted: 23 November 2021

Keywords:
Aerogeophysical measurements; ice shelves; ice thickness measurements; radio-echo sounding; subglacial lakes

Author for correspondence:
Dustin M. Schroeder
E-mail: dustin.m.schroeder@stanford.edu

cambridge.org/jog

Radiometric analysis of digitized Z-scope records in archival radar sounding film

Dustin M. Schroeder[1,2], Anna L. Broome[2], Annabel Conger[1], Acacia Lynch[1], Emma J. Mackie[1] and Angelo Tarzona[1,3]

[1]Department of Geophysics, Stanford University, Stanford, CA, USA; [2]Department of Electrical Engineering, Stanford University, Stanford, CA, USA and [3]School of Earth and Atmospheric Sciences, Georgia Institute of Technology, Atlanta, GA, USA

Abstract

The earliest airborne geophysical campaigns over Antarctica and Greenland in the 1960s and 1970s collected ice penetrating radar data on 35 mm optical film. Early subglacial topographic and englacial stratigraphic analyses of these data were foundational to the field of radioglaciology. Recent efforts to digitize and release these data have resulted in geometric and ice-thickness analysis that constrain subsurface change over multiple decades but stop short of radiometric interpretation. The primary challenge for radiometric analysis is the poorly-characterized compression applied to Z-scope records and the sparse sampling of A-scope records. Here, we demonstrate the information richness and radiometric interpretability of Z-scope records. Z-scope pixels have uncalibrated fast-time, slow-time, and intensity scales. We develop approaches for mapping each of these scales to physical units (microseconds, seconds, and signal to noise ratio). We then demonstrate the application of this calibration and analysis approach to a flight in the interior of East Antarctica with subglacial lakes and to a reflight of an East Antarctic ice shelf that was observed by both archival and modern radar. These results demonstrate the potential use of Z-scope signals to extend the baseline of radiometric observations of the subsurface by decades.

1. Introduction

Ice penetrating radar sounding is one of the most powerful and widely used geophysical techniques in glaciology (Dowdeswell and Evans, 2004). Analysis of geometric information in radar sounding data has been used, for example, to analyze subglacial topography, ice-flow history and ice-shelf melt (Bingham and Siegert, 2007). Radiometric analysis of the same data has also enabled observations of subglacial and englacial hydrology, ice-sheet temperature, and basal roughness among a wide variety of other conditions and processes that are critical for understanding and projecting future sea levels (Scambos and others, 2017; Schroeder and others, 2020). Some of the earliest ice penetrating radar data were collected in the 1960s and 70s from airborne surveys and recorded on optical film (Bailey and others, 1964; Evans and Robin, 1966; Crabtree and Doake, 1986; Gudmandsen, 1975). Recent work digitizing and analyzing archival radar film has demonstrated the potential to compare ice-sheet subsurface geometry in modern and archival radar sounding data over multiple decades (Schroeder and others, 2019) However, due to a lack of radiometric calibration, these studies have been limited to visual interpretations of features such as subglacial lakes (Siegert and Ridley, 1998), basal channels (Le Brocq and others, 2013), and ice shelf geometry (Khazendar and others, 2016).

The Scott Polar Research Institute/National Science Foundation/Technical University of Denmark (SPRI/NSF/TUD) airborne radar sounding surveys of Antarctica in the 1960s and 70s (Drewry and Jordan, 1980; Turchetti and others, 2008) and the contemporaneous surveys of Greenland (Gudmandsen, 1975; Kuiven, 1975) recorded radar sounding data onto 35 mm optical film (Fig. 1). These profiles were the basis of the first subglacial bed maps (Drewry and Jordan, 1980; Lythe and Vaughan, 2001) and early geological and glaciological interpretations (Dowdeswell and Evans, 2004). However, in order to fit those profiles onto the finite dynamic range of optical film while preserving the visibility and interpretability of englacial layers and the bed, along-flight depth profiles called Z-scopes were processed using log-detection, fast-time differentiation and compressive limiting (Fig. 2). By contrast, these surveys also recorded A-scope records. A-scope signals, which passed through the same log-detection receivers as the Z-scope signals, but not the differentiator or limiter.

A-scope traces were recorded every 15 or 20 s (depending on the season) at each increment of the internal Coded Binary Decimal (CBD) counter corresponding to about every 1.5 or 2 km along-track. The CBD counter was used to cross-register the radar and positioning data and was recorded on the film along with the date, time, flight number and mode (Christensen, 1970; Christensen and others, 1970; Skou and Sondergaard, 1976). In order to enable the radiometric comparison of subsurface conditions (such as englacial water storage, hydrology, attenuation and reflectivity) (Christianson and others, 2016; Chu and others, 2016; Schroeder and others, 2016; Kendrick and others, 2018) on similar timescales, in this paper, we develop and demonstrate an approach for the extraction of bed echo power in units of

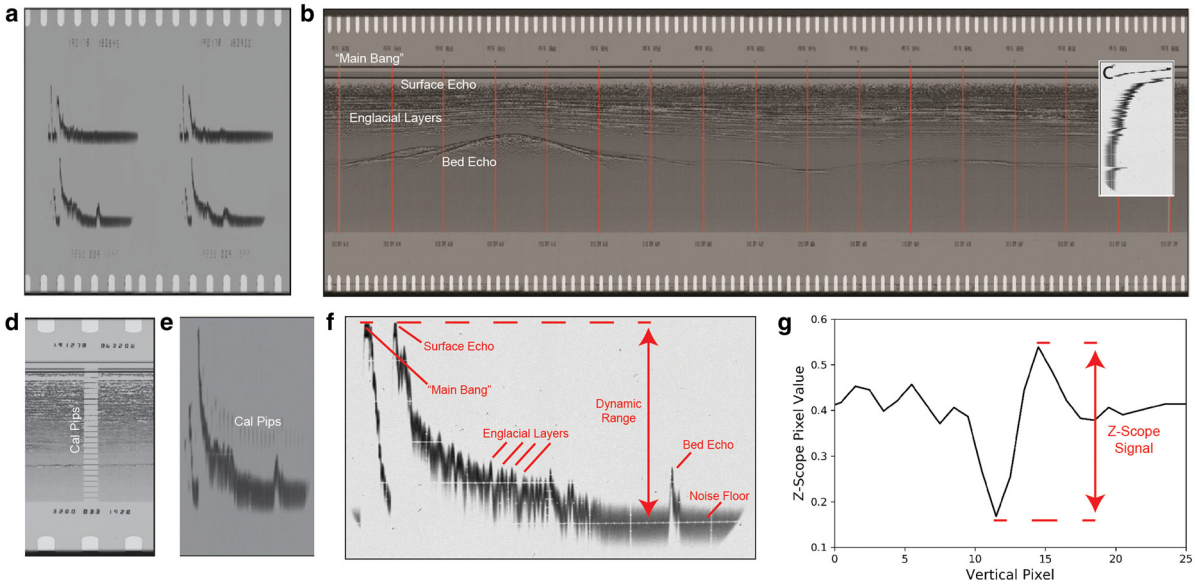

Fig. 1. Scans of 35 mm archival radar film include (a) dual (and single) frequency A-scope traces and (b) Z-scope profiles. The red vertical lines in (b) show the CBD counter interval where A-scope traces are recorded and (c) show an A-scope trace rotated 90 degrees and scaled (Gorman and Siegert, 1999, after) to align with Z-scope traces. Intermittent 'cal pips' in both the (d) Z-scope and (e) A-scope records provide 2 microsecond fast-time calibration. (f) Bed (or other) echo strengths can be calibrated within the dynamic range (A_{scale}) of A-scopes by measuring the vertical number of pixels between the saturated 'main bang' and the noise floor. (g) Z-scope signal strengths can be measured by as the difference between the opposite-signed peaks produced by differentiation within the receiver (see section 2.3). The film segments in this figure were selected to illustrate the types of film records and are not from a single or particular location.

equivalent A-scope signal to noise ratio (SNR) and the production of relative reflectivity profiles from Z-scope records.

Z-scope records are also registered to the date, the time, mode, flight number, and CBD. Although these counters allow the film records to be geolocated, assuming positioning data are available, neither the Z-scope nor A-scope records have absolute power scales. The A-scope records are power traces. As such, utilizing their radiometric information is only a matter of calibrating their power scale. In contrast, the calibration of Z-scopes requires understanding and correcting for the conversion from A-scope signal to fast-time derivatives as well as the compression imposed by the differentiator, limiter and film itself.

There were early pioneering studies with A-scope records which utilized their radiometric information. These include single-trace analysis of subglacial lakes (Gorman and Siegert, 1999), spatial analysis of echoes across the Ross Ice Shelf (Neal, 1982) and studies of internal layering and ice fabric (Siegert and Fujita, 2001; Siegert and Kwok, 2000). Performing this type of analysis with modern scans of the film data requires: (1) calibrating the vertical scale of A-scopes (in microseconds), (2) identifying bed echoes and surface echoes in A-scope traces (using Z-scopes to aid in their identification), and (3) calibrating the power scale of A-scopes (in dB). Expanding this type of analysis to the more spatially continuous Z-scope records requires the additional steps of: (4) determining the relationship of A-scope signals (in dB) to Z-scope signals including the effects of Z-scope compression. In this paper, we develop and present a procedure for performing these calibration steps.

Our radiometric calibration of both A-scope and Z-scope records depends on the parameter A_{scale} which describes the dynamic range of the A-scope SNR (in dB) and which we estimate using bench-top tests published in Christensen (1970); Christensen and others (1970); Skou and Sondergaard (1976) (see section 2.2). A_{scale} is controlled by a portion of the SPRI/NSF/TUD receiver that is not user-adjustable (Christensen, 1970; Christensen and others, 1970; Skou and Sondergaard, 1976) and is therefore expected to remain stable within and across field-seasons.

Our radiometric Z-scope calibration includes the additional empirical fitting of calibrated A-scope and uncalibrated Z-scope bed echoes (see section 2.4). This fitting is done using a logistic function which approximates the user-adjustable Z-scope receiver response. As a result, this calibration can change between, and within, survey lines. Therefore, investigators need to visually inspect Z-scope segments for signs of setting changes (e.g. step-changes in the saturation level or contrast of the Z-scope radargrams) and/or perform sub-segment or cross-segment tests to confirm that those parameters are stable. While this can be a labor-intensive (and at times subjective) sanity-checking process, the fact that these parameters change in discrete increments makes it tractable. Most significantly, our paper shows that within (and between) Z-scope profiles where the parameters describing receiver saturation are stable, the radiometric signature of relative reflectivity can be estimated and interpreted from Z-scope records.

2. Methods

2.1 Geometric calibration

Although Z-scopes are more challenging than A-scopes to calibrate radiometrically, they are better suited for initial visual interpretation and identification of bed and surface interfaces. Z-scope traces can be associated with the individual A-scope measurements using the CBD counter. The vertical red lines in Figure 1b show the locations and spacing of CBD markers where A-scope traces are recorded along a continuous Z-scope profile.

In terms of fast-time calibration, both record types include calibration pips or 'cal pips' recorded every 2 microseconds. In Z-scope records, they appear as horizontal lines along a vertical ruler (Fig. 1d), and in A-scope records, they appear as vertical lines superimposed on the A-scope trace itself (Fig. 1e). The presence of these marks on both types of records enables the cross-calibration of the vertical scale of a Z-scope to the horizontal time axis of A-scopes and both to physical units of time (in microseconds).

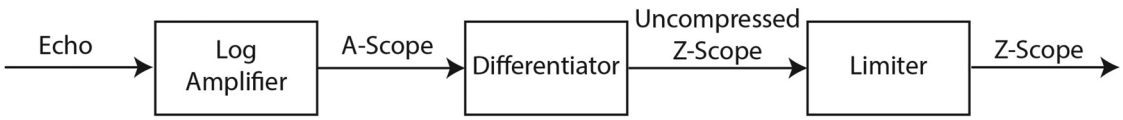

Fig. 2. Flow chart of the radiometrically significant steps in producing the A-scope and Z-scope signals recorded on the 35 mm optical film (Christensen, 1970; Christensen and others, 1970; Skou and Sondergaard, 1976).

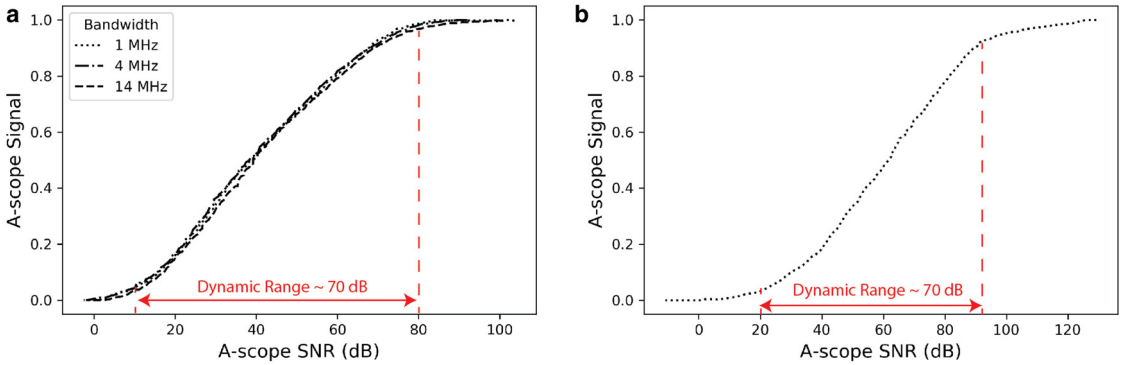

Fig. 3. (a) 60 MHz and (b) 300 MHz A-scope saturation curves from benchtop loop-back tests with variable attenuation (Christensen, 1970; Christensen and others, 1970; Skou and Sondergaard, 1976).

Picking the Z-scope bed and surface follows the common visual interpretation process used in modern radar sounding data and does not require radiometric calibration to be performed. There are automatic picking algorithms for radar sounding data (Panton and Karlsson, 2015, e.g.) but the most common approach is semi-automated picking in which a human interpreter picks two bounds, one above and one below the bed or surface interface and then an automatic re-picker selects the highest power echo between those bounds. However, because Z-scopes are produced by taking the fast-time derivative of A-scope echo power, a radar echo will show up as two sequential opposite-signed peaks in the Z-scope (Fig. 1g). As a result, the automated portion of picking Z-scope data involves selecting the largest Z-scope signal (or positive-to-negative difference) rather than the largest peak. This includes first measuring the number of pixels between positive and negative peaks in a particular scanned Z-scope image (3, e.g., in Fig. 1g) and then identifying the largest difference (within the manual picking bounds) across that number of vertical pixels.

Once Z-scope picks have been recorded, the delay between the bed and surface can be used to identify bed echoes in A-scope traces. In order to do so, the surface return must first be identified in the A-scope record. The left side of an A-scope record (e.g. Fig. 1f) corresponds to the shortest fast-time delay after transmission and the first strong signal is usually the 'main bang' caused by leakage between the transmitter and receiver (or another artifact of the transmission event itself). This is discernible from the surface return because it has a fixed delay and strength across many observations, as is evident in both A-scope and Z-scope records. The surface return is usually followed by a decay in echo power until the bed echo. The bed echo is usually followed by the relatively constant noise floor power level. Once the surface return is identified, the delay at each CBD can be used to identify the bed echo in the A-scope traces.

2.2 A-scope signal, saturation and calibration

Although A-scopes directly record log-detected received power, they do not contain a radiometric calibration reference. Fortunately, the dynamic range of A-scope records can be used to radiometrically calibrate echoes within A-scope traces. Figure 3 is the result of bench-top loop-back testing of the receiver with an in-line variable attenuator (Christensen, 1970; Christensen and others, 1970; Skou and Sondergaard, 1976) and shows a typical amplifier response starting with a noise floor at low input levels, increasing linearly, and saturating at high input levels (Pozar, 2011). We adapted Figure 3 from Christensen (1970); Christensen and others (1970); Skou and Sondergaard (1976) by assuming that the highest A-scope values measured in the test were at saturation and that the lowest values were at the noise floor. As a result, the vertical pixel range in A-scopes (e.g. Fig. 1f) can be converted into A-scope SNR values by picking the noise floor and setting the SNR value of that vertical pixel to be 0 dB, picking the 'main bang' and setting the SNR value of that vertical pixel to $A_{\text{scale}} = 70$ dB (Fig. 3) (Christensen, 1970; Christensen and others, 1970; Skou and Sondergaard, 1976), and linearly interpolating (in dB) between these values.

With the y-axis of A-scopes calibrated in term of A-scope SNR (in dB), A-scope records can be used to perform the same kind of relative, along-profile echo-power, attenuation and reflectivity analysis common in modern digital radar sounding data (Schroeder and others, 2020). However, A-scope traces are recorded only every 1.5 or 2 km and can therefore only be used to observe reflectivity patterns that would not be aliased by such sparse spatial sampling. Given the significant variability between individual radar traces on scales of 2 km and below, A-scope reflectivity patterns should be interpreted either at the scale of profiles, catchments or ice shelves (Neal, 1982, e.g.) or, with great care, as single traces (Gorman and Siegert, 1999, e.g.). However, despite these caveats, the pioneering A-scope based analysis of relative reflectivity and echo character of the Ross Ice Shelf by Neal (1982) is just now being matched by modern data (Tinto and others, 2019).

2.3 Z-scope signal

Z-scope records are produced by differentiating log-detected A-scope signals in fast-time resulting in sequential opposite-signed peaks for a single echo (Fig. 1g). The vast majority of the SPRI/NSF/TUD survey (and surveys of Greenland from the

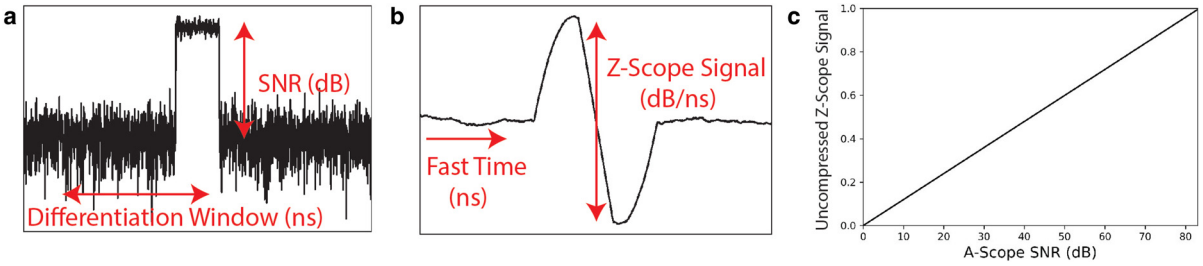

Fig. 4. (a) Simulated A-scope echo with red arrows showing the A-scope SNR (in dB) and the fast-time differentiation window (in ns) used to calculate the (b) simulated Z-scope signal (in dB/ns). (c) These simulations show that, without compression effects from the actual differential amplifier, limiter, and film, Z-scope signals vary linearly with A-scope SNR. The vertical scale in (c) is normalized to the range of SNR values used in the simulation.

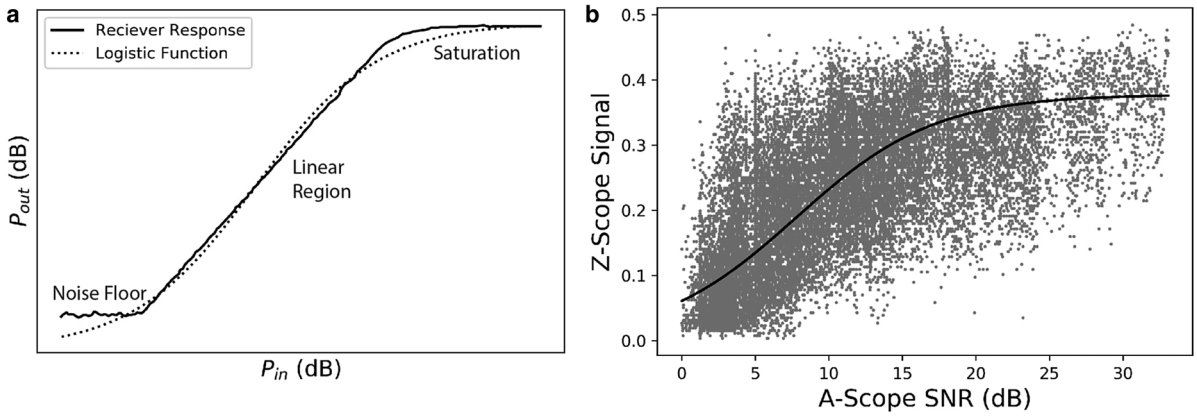

Fig. 5. (a) Generic response of a receiver (adapted from Pozar, 2011), showing the output power (P_{out}) as a function of input power (P_{in}) including the noise floor, linear and saturation regions of that response. The dotted lines illustrate the one realization of a logistic function, which we use to approximate that response. (b) Observed Z-scope signal strength as a function of A-scope SNR for the profile in Figure 6. The black line shows the logistic curve used to estimate the effect of compression for the Z-scope signal along this profile.

same period) were collected in a short-pulse (rather than chirped) mode so that the pulse-length (rather than the waveform) determined the system bandwidth and range resolution (Christensen, 1970; Christensen and others, 1970; Kuiven, 1975). In this configuration, Z-scope signals can be treated as the fast-time derivatives of a square-wave with a 'height' equal to the A-scope SNR (in log-detected A-scope units of dB) resulting in Z-scope signals with units of dB/ns. To illustrate this, we simulate Z-scope signal strength as a function of A-scope SNR using the A-scope geometry in Figure 4a and calculate the Z-scope signal (Fig. 4b) as its fast-time derivative. Figure 4c illustrates the 1 to 1 mapping of A-scope SNR to Z-scope signal before compression. This intuitive relationship is the result of the fast-time differentiation calculating a slope for which the A-scope SNR is the vertical component.

2.4 Z-scope saturation and calibration

Z-scope records also pass through a differential amplifier, limiter and are recorded on film, the net effect of which is to compress the Z-scope signal (Christensen, 1970; Christensen and others, 1970; Kuiven, 1975). In order to calibrate that compression, we utilize a segment of radar sounding data collected in the Gamburtsev Mountain region of interior East Antarctica, which is an ideal area for calibration because the significant relief in ice thickness produces a wide range of bed echo strengths across the dynamic range of both the A-scope and Z-scope records. To empirically constrain and correct for Z-scope compression, we plot the calibrated A-scope SNR (as described in section 2.2) and Z-scope signal for bed echoes along this profile as a scatter plot (Fig. 5b) and approximate the receiver response (Pozar, 2011) including compression due to the differential amplifier and limiter (see Supplementary Materials) as a logistic function (Fig. 5a) given by

$$Z = \frac{A}{\left(1 + e^{B(A_{\mathrm{SNR}} + C)}\right)}, \tag{1}$$

where Z is the Z-scope signal strength, A_{SNR} is the calibrated A-scope SNR, A is the max value, B is the growth rate, and C is the sigmoid mid point. Fitting the curve in Figure 5b yields values of $A = 0.378$, $B = -0.212$ and $C = -7.78$ for Equation (1). Since A-scope traces are acquired much more sparsely than Z-scope signals (Fig. 1b), Z-scope signal strengths are compared to interpolated A-scope SNR values (as shown in Fig. 6). As a result, the spread in Figure 5b is due to the along-track variability in Z-scope bed echo power (due to noise, speckle and clutter as well as changing bed reflectivity and roughness) and the coarse spatial sampling of A-scope traces rather than the receiver compression itself (which is a smooth, deterministic function with unknown parameter values). As a result, the impact of the scatter in Figure 5b is increased uncertainty in the estimations of the parameters (A, B and C) in the saturation function rather than the introduction of a stochastic character to the receiver itself. With A, B and C estimated, Equation (1) can be used to convert the more spatially continuous Z-scope records into equivalent A-scope SNR values.

3. Results

3.1 Z-scope reflectivity signatures of subglacial lakes

Even though the deep interiors of sheets are relatively stable and unlikely to exhibit large radiometric changes between radar film

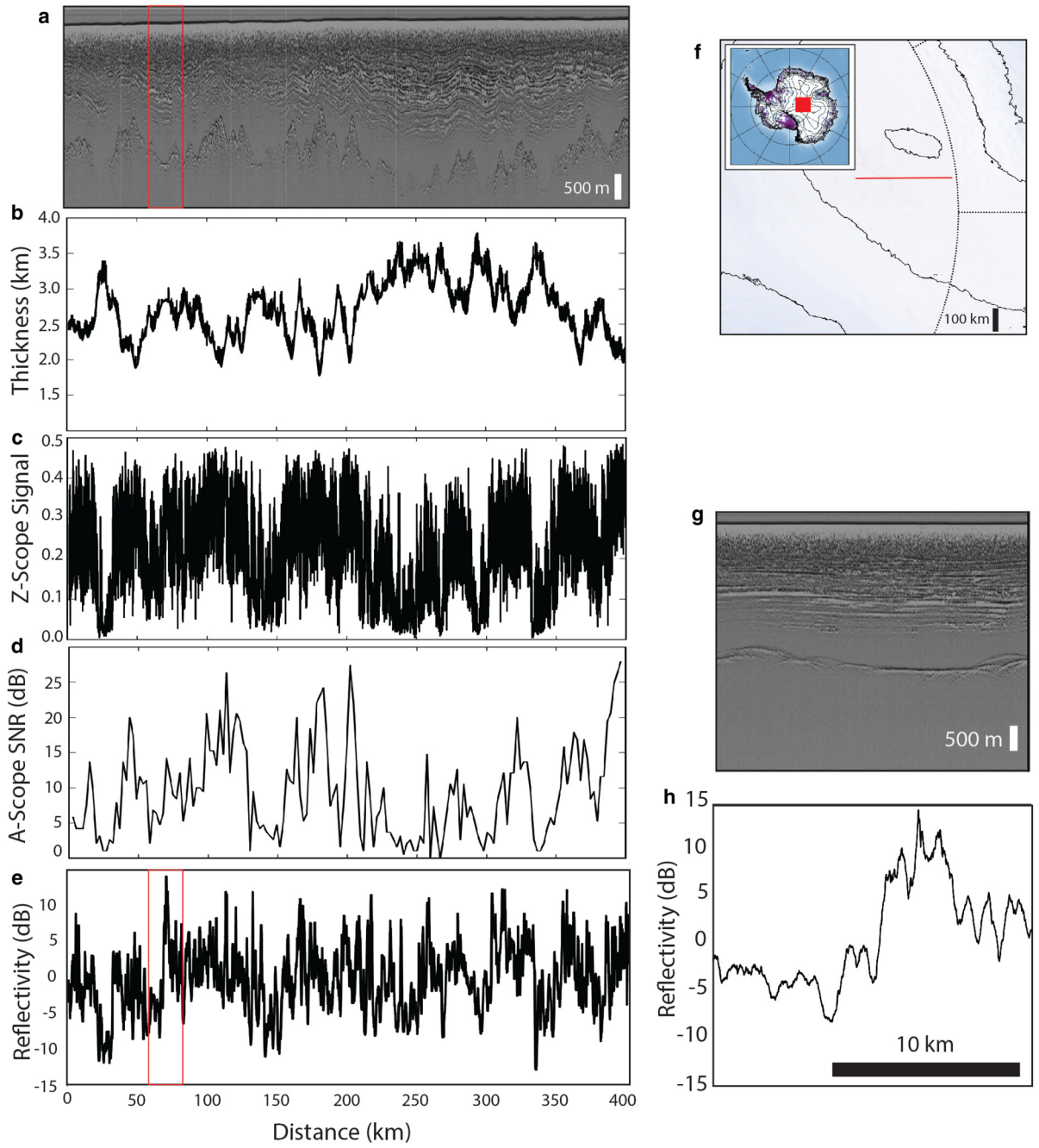

Fig. 6. (a) A Z-scope profile from the Gamburtsev Mountain region of East Antarctica (f) along with (b) extracted ice thickness, (c) Z-scope signal, (d) calibrated A-scope SNR (in dB) and (e) calculated Z-scope relative reflectivity profiles. The red lines correspond to the span of the zoomed-in Z-scope of a single subglacial lake (g) and its corresponding reflectivity signature (h).

records and modern data, they are compelling regions for initial demonstration of Z-scope signal extraction, calibration and analysis. As mentioned above, they exhibit significant ice-thickness relief, which enables the empirical calibration of and correction for attenuation (e.g. Schroeder and others, 2016) and host many stable subglacial 'radar lakes' (MacKie and others, 2020). These lakes are among the brightest, earliest and least ambiguous subglacial radiometric signatures in radar sounding data (Oswald and Robin, 1973; Siegert and others, 2005; Wolovick and others, 2013; Rutishauser and others, 2018).

For this analysis, we use the same flight segment (Fig. 6) from the Gamburtsev Mountains region described above. Visually, the Z-scope radargram in Figure 6a shows the characteristically flat, bright signatures of subglacial lakes (Carter and others, 2007) in the mountain valleys (Wolovick and others, 2013, consistent with). We use Equation (1) and the estimated saturation parameters for this profile to convert the Z-scope signal (Fig. 6c) to its equivalent A-scope SNR values and used these values, along with thickness (Fig. 6b) to calculate the attenuation rate. We follow common radioglaciological practice (Jacobel and others, 2009; Schroeder and others, 2016) and calculate the attenuation rate (in dB/km) as a slope fit to bed power vsthickness. For the profiles in Figure 6, this leads to an estimated one-way depth-averaged attenuation rate $\langle N \rangle = 4.7$ dB/km, which is consistent with modeled values for the region (Matsuoka and others, 2012). Using this attenuation rate, we correct for the total attenuation and calculate the relative (mean adjusted) along-track reflectivity (Fig. 6e). This results in a (99 percentile) range of reflectivity values of 28.9 dB, which is compatible with those theoretically and empirically observed in modern sounding data (Christianson and others,

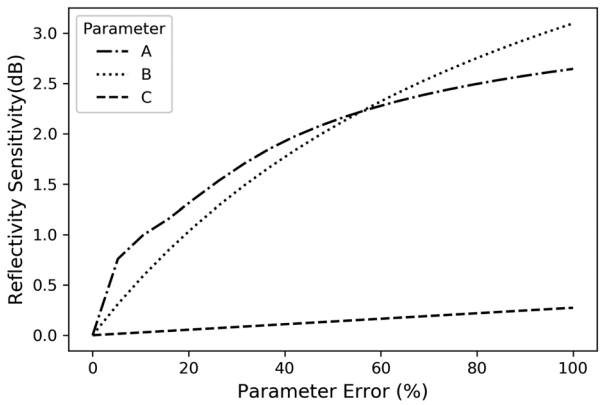

Fig. 7. The sensitivity (RMS error) of the estimated relative reflectivity for the profile in Figure 6 as a function of errors in the parameters (*A*,*B*,*C*) in Equation (1).

2016). The highest reflectivity values in Figure 6 and the portions of the radargrams to which they correspond are consistent with the canonical signatures of subglacial 'radar lakes' (Siegert and Ridley, 1998; Carter and others, 2007; Wolovick and others, 2013; MacKie and others, 2020)

In order to explore the effect of uncertainty in *A*, *B* and *C* on the relative reflectivity signal (e.g. Fig. 6e), we introduce a range of errors (from 0 to 100%) to each of the parameters and calculate the resulting relative reflectivity. We then plot the sensitivity of the calculated relative reflectivity to errors in each of the fitting parameters (Fig. 7) in terms of the 'reflectivity sensitivity' or the root mean squared (RMS) difference between the perturbed and unperturbed relative reflectivity profiles. The modest values in Figure 7 indicate that the relative reflectivity signal (Fig. 6e) can be larger than the uncertainty introduced by even significant (e.g. 100%) errors in the estimated logistic parameters with larger reflectivity errors occurring at higher Z-scope values due to shape of the logistic function itself (Fig. 5b).

The variety of system configurations, surveys, and targets as well as film processing, preservation and digitization across corpus of archival radar film (Gudmandsen, 1975; Drewry and Jordan, 1980; Björnsson and Pálsson, 2020) means that realized uncertainty in any radiometric analysis will depend on the particular features and film under consideration. However, individual researchers can evaluate that uncertainty for their analysis by comparing calibration/fitting-based uncertainties as presented above (e.g. Fig. 7) with the uncertainty/variability/noise in extracted Z-scope signals (as expressed in Fig. 6c and the vertical spread in Fig. 5). In practice, as with modern digital data (Chu and others, 2021), this latter target/environment-based uncertainty is likely to be the dominant source of uncertainty in relative signals for most studies.

3.2 Z-scope reflectivity signatures of an ice shelf

While the ice-sheet interior is ideal for demonstrating the radiometric extraction and calibration because of significant ice-thickness relief and easily identifiable features like subglacial lakes, the interior is less likely to exhibit change on the scale of decades spanned by modern and archival data. Such multi-decadal subsurface evolution is more likely nearer to the coast where active subglacial hydrology (Chu and others, 2016), grounding zones (Christianson and others, 2016) and ice shelves (Khazendar and others, 2016) are undergoing relatively rapid change. Some ice shelves were observed and investigated in the original SPRI/NSF/TUD survey (Neal, 1982; Crabtree and Doake, 1986) and fortunately, there was a near repeat observation of a 1977 SPRI/NSF/TUD flight by the University of Texas Institute for Geophysics (UTIG) High Capability Airborne Radar Sounder (HiCARS) system (Young *et al.*, 2011) in 2011 (Fig. 8a). The archival (Fig. 8b) and modern (Fig. 8d) radargrams are visually and geometrically similar, with the same general bed, ice-shelf and crevasse generated clutter geometries.

We follow the same calibration approach described in 2.4 to confirm that the values for *A*, *B*, and *C* did not change significantly for this survey segment and used these values to calibrate Z-scope signal strength to A-scope equivalent SNR values. We again followed the same attenuation-fitting approach (Jacobel and others, 2009, e.g.) described in section 3.1 to calculate attenuation rates for both the Z-scope (Fig. 8b) and HiCARS (Fig. 8d) profiles. We used the mean value of $\langle N \rangle$ (11.6 dB/km), which is also consistent with modeled values (Matsuoka and others, 2012) for the region, to calculate both relative reflectivity profiles (Figs 8c,e). Notably, our results show that the pattern and strength of the archival (Fig. 8c) and modern (Fig. 8e) reflectivity signals are similar, with the floating ice shelf about 10–20 dB higher than the grounded ice (Christianson and others, 2016, consistent with) and rising toward the center of the shelf. Because this is not an exact reflight, some of the finer-scale differences may be due to temporal change, spatial variationor a combination of the two. However, what is clear is that the general pattern and magnitude of basal reflectivity is consistent across two systems with different signal and processing parameters (albeit with the same center frequency) and recorded on different media (film vs digital records) more than three decades apart.

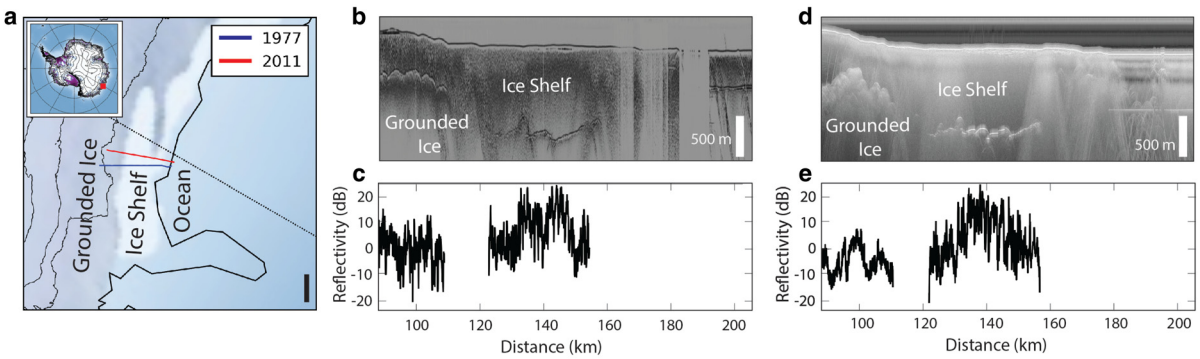

Fig. 8. (a) Location of near-repeat surveys of an East Antarctic ice shelf along the Sabrina Coast, collected by the NSF/SPRI/TUD survey in 1977 (Drewry and Jordan, 1980; Schroeder and others, 2020) and the UTIG HiCARS system in 2011 (Young and others, 2011). (b) Z-scope radargram and (c) Z-scope reflectivity from an NSF/SPRI/TUD survey in 1977 (Drewry and Jordan, 1980; Schroeder and others, 2020) and (d) radargram and (e) reflectivity from a 2011 HiCARS survey (Young and others, 2011).

4. Discussion

The results presented above provide an initial demonstration and a basic understanding of how radiometric information in A-scope and Z-scope records was captured in the NSF/SPRI/TUD archival film record. By leveraging that understanding, we were able to extract, calibrate and interpret geometric and radiometric signals between A-scope and Z-scope records and convert compressed Z-scope signals into equivalent of A-scope SNR values. By converting fast-time measurements of delay into thickness (assuming an index of refraction for ice) and using the A-scope equivalent SNR values extracted from Z-scope records, we were then able to produce interpretable relative reflectivity profiles. In the deep East Antarctic interior, these relative reflectivity values reproduced the empirical strengths, forms and characters of subglacial lakes in modern data (i.e. ~10 dB jumps in the relative reflectivity and increased power variability over visually flat basal interfaces) (Carter and others, 2007; Wolovick and others, 2013; Jordan and others, 2018). Additionally, across an East Antarctic Ice Shelf, the Z-scope based relative reflectivity matched both the general modern radiometric signature of ice shelves (Greenbaum and others, 2015; Khazendar and others, 2016) and the specific pattern of a modern near-reflight of the archival film line (Drewry and Jordan, 1980; Schroeder and others, 2019; Young and others, 2011). Overall, we believe that these results provide a promising proof-of-concept demonstration of the radiometric information richness and interpretability of Z-scope signals and hope that this provides the motivation and basis of significant future work. In addition to greater scientific exploration and utilization of the NSF/SPRI/TUD radar film archive, we believe that there is also compelling follow-on work in the areas of survey-wide calibration, targeted reflights, and the application of these approaches to archival radar film from Greenland (Gudmandsen, 1975; Kuiven, 1975).

In terms of calibration, this paper demonstrates the possibility and process of calibrating individual sounding profiles on a segment-by-segment basis where radar system settings were documented to be stable across significant portions of flights or even across campaigns (Christensen, 1970; Christensen and others, 1970; Skou and Sondergaard, 1976). Although it is currently necessary for investigators to check that *A*, *B*, and *C* are stable across the collection of profiles used in a given study, it should be possible to detect setting changes as step-functions in calibration values along flights and across surveys using a larger portion of the radar film archive. This would likely require leveraging optimization approaches. However, it has the potential to provide better-constrained and survey-wide calibration values.

This paper also provides a first demonstration of quantitative radiometric cross-interpretability between archival radar film and modern data. Quantitative analysis of direct reflights are rare, even in modern data(Chu and others, 2016; Khazendar and others, 2016; Schroeder and others, 2018), but they provide a unique window into the temporal evolution of subsurface conditions. With portions of SPRI/NSF/TUD surveys collected 50 years ago (Schroeder and others, 2019), contemporary reflights of these lines (especially in more rapidly changing regions) could provide a window into subsurface processes at the half-century timescale. Given the criticality of decadal-scale predictions for climate adaptation and the widespread use of a century as a planning baseline in reports like the International Panel on Climate Change (IPCC) (Solomon, 200; Scambos and others, 2017; Kennicutt and others, 2019), the ability to observe subsurface conditions over five decades could enable deeper understanding of critical processes and inform numerical modeling used in sea-level projections.

Finally, the successful extraction and analysis of radiometric signals from Z-scope profiles stand to enable the application of modern radiometric analysis techniques to archival film data. For example, in dynamic areas of the Greenland Ice Sheet, interaction between supraglacial and englacial hydrology plays a critical, but poorly understood, role in the dynamic response of Greenland ice flow to surface melt (Moon and others, 2014). Other work has demonstrated that the synthesis of ice-sheet modeling and radar sounding data can estimate water storage and firn aquifers thickness from airborne surveys (Chu and others, 2018). Applying these analysis techniques to the radar sounding film archive of data collected in Greenland in the 1960s and 70s (Gudmandsen, 1975; Kuiven, 1975) could enable a multi-decadal window into the evolution of englacial hydrology across the Greenland Ice Sheet.

5. Conclusion

In this paper, we demonstrated geometric fast-time and slow-time calibration of the A-scope and Z-scope record types in archival radar sounding film and radiometrically cross-calibrate Z-scope signal strength with A-scope SNR values. These calibrations can be performed on any of the archival NSF/SPRI/TUD film for which both A-scope and Z-scope records are available. We demonstrated the successful extraction, calibration and calculation of relative reflectivity values for a profile in the Gamburtsev Mountain region of East Antarctic, producing canonical radiometric signatures of subglacial lakes. In the same manner, we also demonstrated the successful extraction and calculation of a Z-scope reflectivity profile across an East Antarctic ice shelf with similar character and strength to a near-repeat profile from a modern digital radar sounding collected 30 years later. In combination, these results highlight the potential (and provide the technical foundation) for radiometric analysis of Z-scope records in archival radar sounding film and motivate future reflights of archival data to enable radiometric analysis of multi-decadal subsurface evolution.

Supplementary material. The supplementary material for this article can be found at https://doi.org/10.1017/jog.2021.130

Acknowledgements. We thank N. Holschuh and M. Siegert for their thorough, thoughtful, and constructive reviews. This work was supported, in part, by NSF award 1745137, Heising-Simons Foudation Grant 2020-1771, the Stanford Summer Undergraduate Research in Geoscience and Engineering Program, the Stanford Earth Summer Undergraduate Research Program, and the National Defense Science and Engineering Graduate Fellowship Program. The authors would also like to acknowledge Julian Dowdeswell, Lucy Martin and Naomi Boneham of the Scott Polar Research Institute at the University of Cambridge for their partnership in scanning the radar film archive.

References

Bailey JT, Evans S and Robin GdQ (1964) Radio echo sounding of polar ice sheets. *Nature* **204**(4957), 204420a0.

Bingham RG and Siegert MJ (2007) Radio-echo sounding over polar ice masses. *Journal of Environmental & Engineering Geophysics* **12**(1), 47–62.

Björnsson H and Pálsson F (2020) Radio-echo soundings on icelandic temperate glaciers: history of techniques and findings. *Annals of Glaciology* **61** (81), 25–34.

Carter SP and 5 others (2007) Radar based subglacial lake classification in Antarctica. *Geochemistry, Geophysics, Geosystems* **8**(3), 1–20. doi: 10.1029/2006GC001408.

Christensen EL (1970) Radioglaciology, 300 MHz Redar, Technical University of Denmark.

Christensen EL, Gundestrup N, Nilsson E and Gudmandsen P (1970) Radioglaciology, 60 MHz Radar, Technical University of Denmark.

Christianson K and 6 others (2016) Basal conditions at the grounding zone of Whillans Ice Stream, West Antarctica, from ice penetrating radar. *Journal of Geophysical Research: Earth Surface* **121**(11), 1954–1983.

Chu W and 5 others (2016) Extensive winter subglacial water storage beneath the Greenland Ice Sheet. *Geophysical Research Letters* **43**(24), 12,484– 12,492. doi: 10.1002/2016GL071538.

Chu W and 8 others (2021) Multi-system synthesis of radar sounding observations of the amundsen sea sector from the 2004–2005 field season. *Journal of Geophysical Research: Earth Surface* **26**(10), e2021JF006296.

Chu W, Schroeder DM and Siegfried MR (2018) Retrieval of englacial firn aquifer thickness from ice penetrating radar sounding in Southeastern Greenland. *Geophysical Research Letters* **45**(21), 11770–11778.

Crabtree RD and Doake CSM (1986) Radio-echo investigations of Ronne Ice Shelf. *Annals of Glaciology* **8**, 37–41.

Dowdeswell JA and Evans S (2004) Investigations of the form and flow of ice sheets and glaciers using radio-echo sounding. *Reports on Progress in Physics* **67**(10), 1821.

Drewry DJ and Jordan SR (1980) Compilation of an Antarctic glaciological and geophysical folio. *Polar Record* **20**(126), 288–288.

Evans S and Robin GdQ (1966) Glacier depth-sounding from the air. *Nature* **210**(5039), 883–885.

Gorman MR and Siegert MJ (1999) Penetration of Antarctic subglacial lakes by VHF electromagnetic pulses: information on the depth and electrical conductivity of basal water bodies. *Journal of Geophysical Research: Solid Earth* **104**(B12), 29311–29320.

Greenbaum JS and 10 others (2015) Ocean access to a cavity beneath Totten Glacier in East Antarctica. *Nature Geoscience* **8**(4), 294–298.

Gudmandsen P (1975) Layer echoes in polar ice sheets. *Journal of Glaciology* **15**(73), 95–101.

Jacobel RW, Welch BC, Osterhouse D, Pettersson R and MacGregor JA (2009) Spatial variation of radar-derived basal conditions on Kamb Ice Stream, West Antarctica. *Annals of Glaciology* **50**(51), 10–16.

Jordan TM and 8 others (2018) A constraint upon the basal water distribution and thermal state of the Greenland Ice Sheet from radar bed echoes. *The Cryosphere* **12**(9), 2831–2854.

Kendrick AK and 12 others (2018) Surface meltwater impounded by seasonal englacial storage in West Greenland. *Geophysical Research Letters* **45**(19), 10474–10481.

Kennicutt MC and 28 others (2019) Sustained Antarctic research: a 21st century imperative. *One Earth* **1**(1), 95–113.

Khazendar A and 8 others (2016) Rapid submarine ice melting in the grounding zones of ice shelves in West Antarctica. *Nature Communications* **7**, 13243.

Kuiven K (1975) The Greenland Ice Sheet Program, GISP 1974.

Le Brocq AM and 10 others (2013) Evidence from ice shelves for channelized meltwater flow beneath the Antarctic Ice Sheet. *Nature Geoscience* **6**(11), 945–948.

Lythe MB and Vaughan DG (2001) BEDMAP: a new ice thickness and subglacial topographic model of Antarctica. *Journal of Geophysical Research: Solid Earth* **106**(B6), 11335–11351.

MacKie EJ, Schroeder DM, Caers J, Siegfried MR and Scheidt C (2020) Antarctic topographic realizations and geostatistical modeling used to map subglacial lakes. *Journal of Geophysical Research: Earth Surface* **125** (3), 1–22. doi: 10.1029/2019jf005420.

Matsuoka K, MacGregor JA and Pattyn F (2012) Predicting radar attenuation within the Antarctic ice sheet. *Earth and Planetary Science Letters* **359**, 173–183. doi: 10.1016/j.epsl.2012.10.018

Moon T and 6 others (2014) Distinct patterns of seasonal Greenland glacier velocity. *Geophysical Research Letters* **41**(20), 7209–7216.

Neal CS (1982) Radio echo determination of basal roughness characteristics on the Ross Ice Shelf. *Annals of Glaciology* **3**, 216–221.

Oswald GKA and Robin GDQ (1973) Lakes beneath the Antarctic Ice Sheet. *Nature* **245**(5423), 245251a0.

Panton C and Karlsson NB (2015) Automated mapping of near bed radio-echo layer disruptions in the Greenland Ice Sheet. *Earth and Planetary Science Letters* **432**, 323–331.

Pozar DM (2011) *Microwave engineering*. Hoboken, NJ: John wiley & sons.

Rutishauser A and 8 others (2018) Discovery of a hypersaline subglacial lake complex beneath Devon Ice Cap, Canadian Arctic. *Science Advances* **4**(4), 1–6. doi: 10.1126/sciadv.aar4353.

Scambos TA and 9 others (2017) How much, how fast? A science review and outlook for research on the instability of Antarctica's Thwaites Glacier in the 21st century. *Global and Planetary Change* **153**, 16–34.

Schroeder DM and 9 others (2019) Multidecadal observations of the Antarctic ice sheet from restored analog radar records. *Proceedings of the National Academy of Sciences* **116**(38), 18867–18873.

Schroeder DM and 9 others (2020) Five decades of radioglaciology. *Annals of Glaciology* **61**, 1–13.

Schroeder DM, Hilger AM, Paden JD, Young DA and Corr HFJ (2018) Ocean access beneath the southwest tributary of Pine Island Glacier, West Antarctica. *Annals of Glaciology* **59**(76pt1), 10–15.

Schroeder DM, Seroussi H, Chu W and Young DA (2016) Adaptively constraining radar attenuation and temperature across the Thwaites Glacier catchment using bed echoes. *Journal of Glaciology* **62**(236), 1075–1082.

Siegert MJ, Carter S, Tabacco I, Popov S and Blankenship DD (2005) A revised inventory of Antarctic subglacial lakes. *Antarctic Science* **17**(3), 453–460.

Siegert MJ and Fujita S (2001) Internal ice-sheet radar layer profiles and their relation to reflection mechanisms between Dome C and the Transantarctic Mountains. *Journal of Glaciology* **47**(157), 205–212.

Siegert MJ and Kwok R (2000) Ice-sheet radar layering and the development of preferred crystal orientation fabrics between Lake Vostok and Ridge B, Central East Antarctica. *Earth and Planetary Science Letters* **179**(2), 227–235.

Siegert MJ and Ridley JK (1998) An analysis of the ice sheet surface and subsurface topography above the Vostok Station subglacial lake, central East Antarctica. *Journal of Geophysical Research: Solid Earth* **103**(B5), 10195–10207.

Skou N and Sondergaard F (1976) Radioglaciology, a 60 MHz ice sounder system, Technical University of Demnark.

Solomon S, Manning M, Marquis M, Qin D (2007) *Climate Change 2007 – The Physical Science Basis: Working Group I Contribution to the Fourth Assessment Report of the IPCC*. Cambridge: Cambridge University Press.

Tinto KJ and 30 others (2019) Ross Ice Shelf response to climate driven by the tectonic imprint on seafloor bathymetry. *Nature Geoscience* **12**(6), 441–449.

Turchetti S, Dean K, Naylor S and Siegert M (2008) Accidents and opportunities: a history of the radio echo-sounding of Antarctica, 1958–79. *The British Journal for the History of Science* **41**(3), 417–444.

Wolovick MJ, Bell RE, Creyts TT and Frearson N (2013) Identification and control of subglacial water networks under Dome A, Antarctica. *Journal of Geophysical Research: Earth Surface* **118**(1), 140–154.

Young DA and 11 others (2011) A dynamic early East Antarctic Ice Sheet suggested by ice-covered fjord landscapes. *Nature* **474**(7349), 72–5.